Chapter in **Advancing Astrophysics with the SKA – II**

Solar Radio Burst Fine Structures

Eduard P. Kontar [1], Daniel Clarkson [1], Hamish Reid [2], Yingjie Luo [1], Nicolina Chrysaphi [3,1], Alexey Kuznetsov [4], Galina Motorina [5,6,1] and Carine Briand [7]

[1] *School of Physics & Astronomy, University of Glasgow, G12 8QQ, UK*
[2] *Mullard Space Science Laboratory, UCL, London, UK*
[3] *INAF-IAPS, Via del Fosso del Cavaliere, 100, 00133 Rome, Italy*
[4] *Institute of Solar-Terrestrial Physics, Irkutsk 664033, Russia*
[5] *Central Astronomical Observatory at Pulkovo of Russian Academy of Sciences, St. Petersburg, 196140, Russia*
[6] *Ioffe Institute, Polytekhnicheskaya, 26, St. Petersburg, 194021, Russia*
[7] *LIRA, Observatoire de Paris-PSL, CNRS, Sorbonne Université, Université Paris Cité, Université Cergy, 92190 Meudon, France*
E-mail: Daniel.Clarkson@glasgow.ac.uk, hamish.reid@ucl.ac.uk, nicolina.chrysaphi@inaf.it

Solar radio bursts exhibit intricate variability in time, space, and frequency, often displaying a rich variety of fine frequency-time structures such as spikes, drift pairs, striae in Type III bursts, and herringbone patterns in Type II bursts, etc. Historically, limited spatial, spectral, and temporal resolution has hindered detailed investigation of these narrow-band, rapidly evolving features, restricting progress in identifying their physical origins and underlying processes at these scales. Advances in high-time-frequency-resolution solar imaging now offer transformative opportunities. Recent sub-second imaging spectroscopy has revealed that many fine structures challenge existing theoretical models, pointing to the need for new frameworks and a reassessment of current interpretations. The Square Kilometre Array (SKA), with its full-Stokes imaging spectroscopy at sub-second cadences, will provide unprecedented data essential for resolving these long-standing questions. These capabilities promise to significantly deepen our understanding of electron acceleration and transport, magnetic reconnection, and coronal plasma turbulence, thereby advancing our knowledge of solar energetic processes and improving assessments of their space-weather impacts.

Contents

1 Introduction **2**

2 Spike radio bursts **4**

3 Drift-pair bursts **7**

4 Type III striae **8**

5 Type II bursts fine structures **10**

6 Fine structures within flaring regions **12**

7 Solar observations and further progress **13**

8 Summary **16**

9 Acknowledgements **16**

1 Introduction

During periods of sporadic solar activity, the Sun efficiently converts magnetic energy into the kinetic energy of particles. While similar processes are observed throughout the Universe (e.g., stellar coronae, in planetary magnetospheres and ionospheres, or in accretion disks), solar phenomena are unique due to their proximity, which allows for unprecedentedly detailed studies (e.g. Dennis et al., 2011; Holman et al., 2011; Kontar et al., 2011; Benz, 2017, as reviews). Signatures of energized thermal and non-thermal electrons are observed in hard X-rays, ultraviolet, and radio domains. Among these, radio emission offers unmatched temporal resolution, which is essential for studying solar transient phenomena (see Figure 1 and zoomed in Figure 2, providing a unique high-time-resolution perspective on key questions in solar physics.

One of the most fascinating aspects of solar radio emission is its complexity and variability. Full-Sun spectroscopic observations have catalogued a variety of sub-second, relatively narrow-band features (Chernov, 2011). Notable examples of these fine structures include spikes, fine structures within type I bursts, type IIIb (or stria) bursts, pulsations, and drifting pairs. These features have been studied primarily through spectroscopy, and more recently with imaging-spectroscopy below 50 MHz. However, while dynamic spectra have provided detailed information on fine structures, imaging studies remain scarce or even absent. Notably, imaging observations have sometimes produced unexpected results. For example, early imaging of spikes above 400 MHz (though unresolved in time) by Chernov (2011) suggested that decimetric spikes do not originate from coronal X-ray flare sources, contrary to previous expectations. The first frequency and time resolved observations of spikes (Clarkson et al., 2021; Clarkson and Kontar, 2025) show that the radio source centroid velocities are often superluminal.

The most fascinating features of solar radio emission are its complexity and variability. Using full-Sun spectroscopic observations, the presence of various sub-second and relatively narrow band features has been well catalogued (Chernov, 2011). Bright examples of fine structures are spikes,

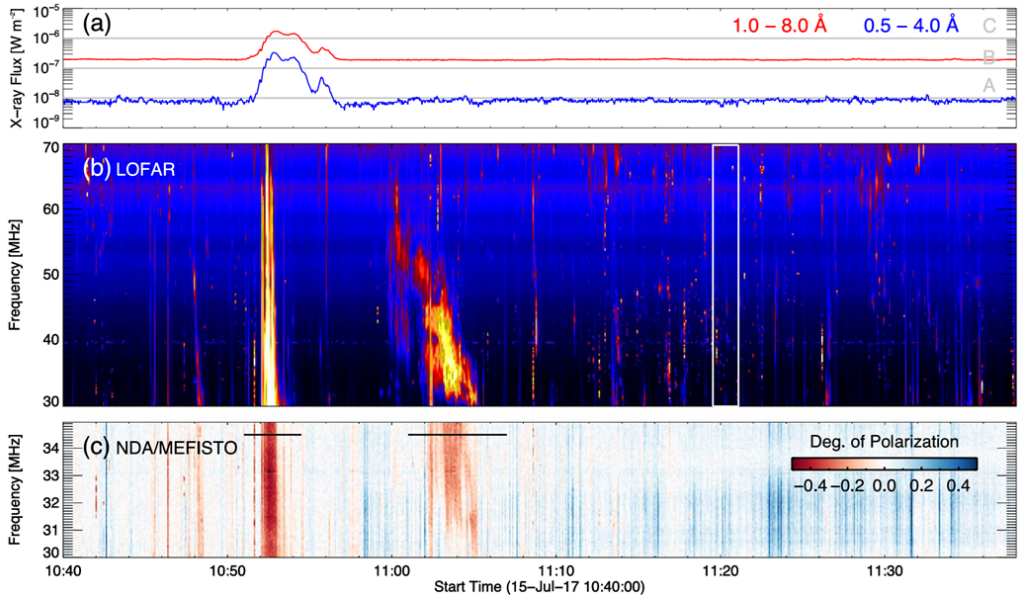

Figure 1: Solar flare with X-ray emission and type III and type II radio emissions. (a) GOES X-ray light curves. (b) LOFAR dynamic spectrum showing a series of bright Type III bursts followed by type II bursts (Chrysaphi et al., 2020) and myriad of fine structures. (c) Dynamic spectrum of the circular polarization from the NDA. The image is adapted from (Clarkson et al., 2021).

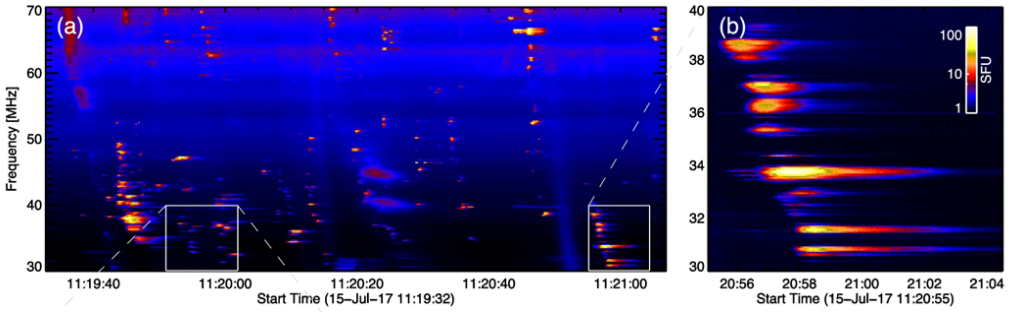

Figure 2: Zoomed in dynamic spectra. (a) Numerous fine structures are visible in the region bounded by white white box in Figure 1 (b) Zoomed-in Type IIIb burst near 11:21 UT. The image is adapted from (Clarkson et al., 2021).

fine structure of type I bursts, Type IIIb (or stria) bursts, pulsations, drifting pairs, etc. These features have been actively studied mostly spectroscopically, and more recently using imaging-spectroscopy below 50 MHz. While the fine structures are well studied using the dynamic spectra, the imaging studies are scarce or non-existent. Importantly, imaging observations often show rather puzzling results. Early imaging observations of spikes above 400 MHz but unresolved in time Battaglia and Benz (2009) suggest that decimetric spikes do not originate from coronal X-ray flare sources contrary to previous expectations. The first frequency and time resolved observations of spikes (Clarkson et al., 2021; Clarkson and Kontar, 2025) show that the radio source centroid velocities are often superluminal.

The main challenge in frequency-time resolved observations of fine structures arises from the high variability of the emission (see Figure 1), which necessitates imaging at many frequencies simultaneously and with high time resolution. Such observations of fine structures have only recently been performed (Kontar et al., 2017) with the Low Frequency Array (LOFAR, van Haarlem et al., 2013). As a result, time-resolved imaging of fine structures has long been a significant challenge.

The Square Kilometre Array (Braun et al., 2019) presents new opportunities for discoveries in solar physics (Nakariakov et al., 2015; Nindos et al., 2019), and in particular for the study of solar radio burst fine structures. This chapter summarizes recent observations and challenges, highlighting the unique opportunities that the SKA will provide.

2 Spike radio bursts

Narrowband, short-duration fine structures known as radio spike bursts are often observed independently of broadband emission, making them a notable phenomenon. They appear across a wide frequency range, from gigahertz (Staehli and Magun, 1986; Benz et al., 1992; Krucker and Benz, 1994; Cliver et al., 2011; Dąbrowski et al., 2011; Chen et al., 2015; Luo et al., 2021) and hundreds of megahertz (Tarnstrom and Philip, 1972a; Guedel and Benz, 1990; Krucker et al., 1995; Bouratzis et al., 2016), down to tens of megahertz (Barrow et al., 1994; Melnik et al., 2014; Shevchuk et al., 2016; Clarkson et al., 2023). Their high brightness temperatures link them to coherent emission mechanisms such as electron cyclotron maser emission (Melrose and Dulk, 1982; Benz et al., 1992) and plasma emission (Tarnstrom and Philip, 1972b; Melnik et al., 2014; Clarkson et al., 2021; Murphy et al., 2024).

The prevalence of spikes, especially at and above decimetre wavelengths, can cause radio interference at Earth, and be particularly problematic for GPS/GLONASS noise (Cerruti et al., 2008; Kintner et al., 2009; Cliver et al., 2011). The spikes occur in several solar activity environment, i.e. noise storms, Type III storm, Type II or Type IV solar radio bursts. At a few hundred MHz frequencies, the spikes could occur with type III bursts at frequencies above the type III starting frequency and can coincide with HXR emission (Guedel et al., 1991). This has led to the view that spikes are a direct signature of the acceleration of non-thermal electrons (Benz et al., 1982). Their sporadic appearance in dynamic spectra can form clusters of thousands of spikes, which may suggest that the acceleration region is fragmented and that energy release could occur across many small sites (Benz, 1985). At decametre frequencies, recent imaging results show that spike bursts share spatial and morphological features with type IIIb striae. This suggests that decametre spikes arise from propagating electron beams and plasma emission, modulated by density fluctuations in the intervening plasma, producing radio emission across narrow spatial regions (Clarkson et al., 2021, 2023).

2.1 Time-frequency characteristics

Spikes are likely the shortest duration radio emissions observed from the Sun at decametre wavelengths. At decimetric frequencies, the timescales are on the order of tens of milliseconds, increasing to hundreds of milliseconds to $\sim$ 1 s at decametre frequencies. Earlier studies linked the brief lifetime of spikes to collisional damping in the plasma (e.g. Guedel and Benz, 1990). However, recent

observations reveal significant radio-wave scattering acting on these sub-second bursts. The decay time of spikes follows a $1/f$ relation across a wide frequency range (Figure 3), consistent with radio-wave scattering theory (Kontar et al., 2023). Near 30 MHz, scattering appears to dominate the observed profiles, suggesting that the intrinsic emission timescale is much shorter on the order of tens of milliseconds rather than $\sim$ 1 s as observed (Clarkson et al., 2021). This suggests that the intrinsic timescale of the emission may be shorter than what is inferred from observations. The SKA's planned temporal imaging resolution of 1 ms will greatly enhance the ability to resolve high frequency spikes over the broad range of frequencies (Figure 3). This capability will enable detailed studies of emission and acceleration timescales in flaring regions, and may also reveal the fine structures that contribute to type I noise storm continua.

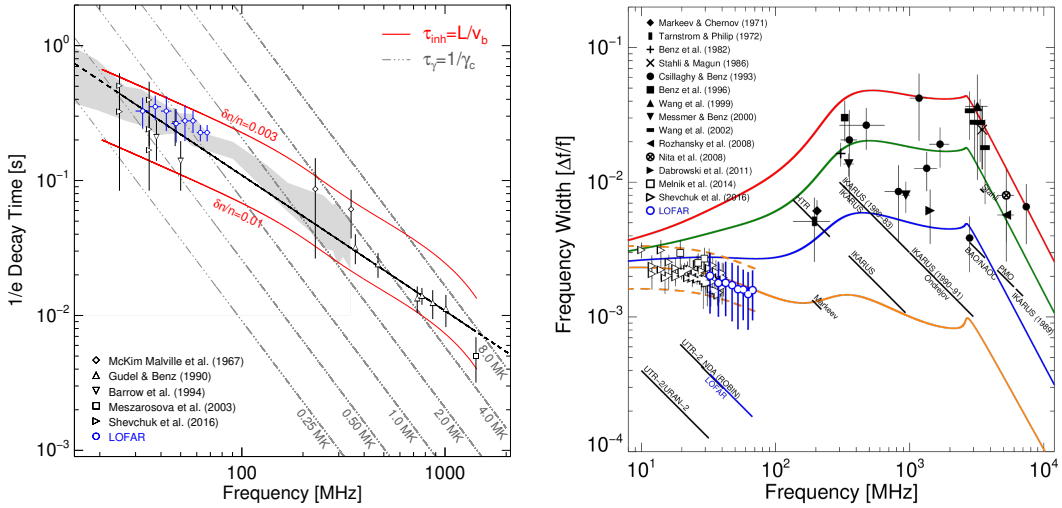

Figure 3: *Left:* Average spike 1/e decay times against frequency. The solid black line represents the power-law fit to the data given by $\tau_d = (11.22 \pm 1.9) f^{-1.01 \pm 0.03}$. The dash-dotted gray lines represent the plasma collision time for various coronal temperatures. The gray region shows the typical scattering decay time where the spread accounts for halving and doubling of the scattering rate (see Kontar et al., 2023). The red curves show the inhomogeneity time. *Right:* Average spike bandwidth ratio $\Delta f/f$ where Δf is given at the FWHM level. The solid black lines show the instrument spectral resolution. The coloured lines denote the bandwidth derived from the Langmuir-wave dispersion relation for various magnetic field profiles. Figures adapted from Clarkson et al. (2023).

Spike bandwidths are typically in the range $\Delta f/f \simeq 10^{-3} - 10^{-2}$, hence often requiring high frequency resolution. They usually have symmetrical profiles in frequency, with bandwidth increasing at higher frequencies. Above $\sim$ 200 MHz, spike bandwidth ratios are an order of magnitude larger than those below 100 MHz. This broadening can be attributed to the Langmuir wave dispersion relation in a magnetized plasma (e.g. Shevchuk et al., 2016; Clarkson et al., 2023), which depends on the local magnetic field strength. However, a major limiting factor in past bandwidth measurements at decimetric frequencies has been the spectral resolution of the observing instruments, which may have led to overestimates in statistical averages (Figure 3). For spikes produced by plasma emission and modulated by density inhomogeneities, the bandwidth can be used to estimate the size of the emitting region (that is, the size of the density inhomogeneity) as $\Delta r \simeq 2L(\Delta f/f)$

where L is a characteristic density scale height (e.g. Kontar et al., 2017). SKA-Low has a standard spectral resolution of 5.4 kHz with a maximum resolution of 226 Hz in zoom mode (Hampson et al., 2022). In combination with imaging, this improvement will allow radio fine structures such as spikes and repeating bursts (Ma et al., 2026) to probe smaller regions of plasma turbulence and help to constrain emission region properties and sizes.

Above a few hundred megahertz, spike frequency drift rates range between $10^2 - 10^4$ MHz s^{-1} and show a similar frequency dependence to type III bursts. Near 30 MHz, however, spike emission is strongly affected by temporal broadening due to radio-wave scattering, which smears the signal in dynamic spectra and reduces the apparent drift-rate (Clarkson and Kontar, 2025). Even with the spectral resolution of LOFAR, decametre spikes tend to cover a modest number of frequency channels (Figure 4), making it difficult to track the drift of the intensity peak across the channels. Using the same approach used type IIIb striae (e.g. Sharykin et al., 2018), Clarkson et al. (2023) measure absolute spike drift rates from near zero to a few tens of kilohertz per second. The dilution of the drift rate affects estimates of the plasma temperature (Clarkson and Kontar, 2025), a key parameter influencing the drift of fine structures produced through the plasma emission process (Reid and Kontar, 2021). The enhanced spectral resolution of SKA-Low will enable more precise tracking of spike peak flux across frequency channels, improving estimates of coronal temperatures and the role of scattering in shaping the observed burst dynamics.

2.2 Imaging

Radio imaging observations of spikes remain limited because few instruments can provide the necessary combination of spatial, spectral, and temporal resolution. The first resolved imaging of spikes was achieved with LOFAR near 30 MHz (Clarkson et al., 2021, 2023), showing that spike source sizes follow radio-wave scattering predictions consistent with strong anisotropy in density turbulence (Kontar et al., 2023, 2025). At a fixed frequency over time, the spike bursts displayed substantial positional shift across the sky-plane — up to nearly a solar radius in less than 1 s along the direction of the guiding magnetic field. This demonstrates the dominant role of radio-wave scattering, which can produce superluminal apparent source motion. The LOFAR observations, performed in beam-formed mode (Gordovskyy et al., 2022), enabled tracking of spike sources on tens of millisecond timescales but with a modest angular resolution of ~ 9 arcmin at 30 MHz. As a result, any substructure within individual bursts or multiple sources could not be resolved.

At 50 MHz, SKA-Low configured with a ~ 6 km baseline would be able to tile a region of 2.5 $R_\odot$ radius centred on the Sun using 500 beams, achieving an angular beam width of 3.5 arcmin—nearly a factor of two improvement over LOFAR's 5.9 arcmin using 217 beams with a 3.5 km baseline. Moreover, convolution of the instrumental beam affects the apparent size and shape of radio sources, and improved angular resolution will improve this distortion. Since source broadening occurs mainly perpendicular to the magnetic field due to anisotropic scattering (Kontar et al., 2019), SKA-Low's enhanced imaging may reveal source orientations that can be used to infer the direction of the magnetic field.

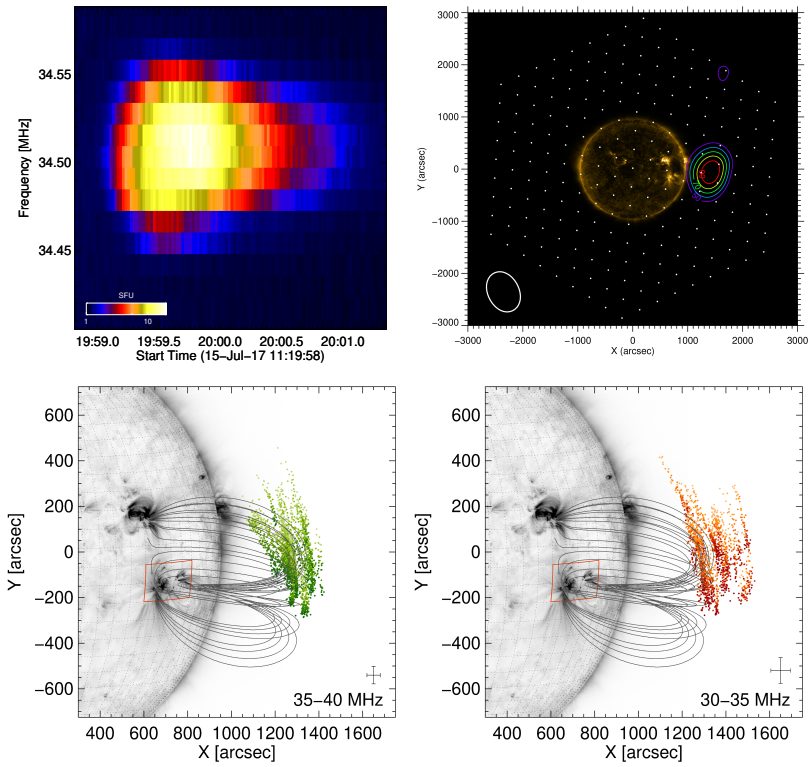

Figure 4: *Top Left:* LOFAR dynamic spectrum of an individual spike. *Top Right:* LOFAR image of the spike peak flux at 34.5 MHz. The oval in the lower left corner represents the beam size. *Lower Left:* LOFAR observed centroid positions of hundreds of spikes between 35-40 MHz with time increasing from dark to light. *Lower Right:* As in the lower left panel but for spikes observed between 30-35 MHz. Lower panels adapted from Clarkson et al. (2023).

3 Drift-pair bursts

Drift-pair bursts are a rare type of fine structure that are observed sometimes in low-frequency solar radio emission (in the frequency range of about 10-100 MHz). They were first identified as a separate class of fine structures by Roberts (1958). The bursts appear in the dynamic spectra as two parallel frequency-drifting narrowband stripes separated in time, with a typical delay between the components of about 1-2 s. The frequency drifts can be both positive (which are more common) and negative. The drift rates tend to increase with the emission frequency, being generally of about 1-2 MHz s^{-1} at the frequency of $\sim$ 30 MHz. The emission intensities are up to hundreds of sfu, and the brightness temperatures exceed 10^{10} K, indicating a coherent emission mechanism. The circular polarization degree varies from very low to $\sim$ 50%. The bursts usually occur not individually, but form large irregular groups (clusters).

3.1 Time-frequency characteristics

The most intriguing feature of drift-pair bursts is their double structure, where the second component of a pair looks like a repetition of the first one with the same frequency range and drift rate, although sometimes with a slightly different intensity. Also, the higher-frequency component generally has

a higher polarization degree. The duration of each component at a single frequency is of $\sim$ 1 s, which corresponds to an instant bandwidth of $\sim$ 1 MHz. The delay between the components tends to decrease slightly with frequency. The bursts with negative frequency drift are usually shorter and more narrowband than those with positive frequency drift.

3.2 Imaging

Suzuki and Gary (1979), using the Culgoora radioheliograph, first discovered that the sources of both components of a drift-pair burst (at the same frequency) coincide spatially. Later, Kuznetsov and Kontar (2019), using multi-frequency imaging observations with LOFAR, have found that the sources of both components of a drifting pair propagate (with a certain delay) in the same direction along the same trajectory. At a fixed frequency, at the decay phases of both components, the emission source demonstrates an outward radial motion (with the speed of about $c/3$) and an increase in size; this behaviour is reminiscent of the source dynamics in type IIIb bursts (Kontar et al., 2017).

Since the first observations, the formation of drift-pair bursts was attributed to the radio echo effect, when the second component represents a signal reflected from lower layers of the solar corona. On the other hand, a direct (regular) reflection in a stratified corona cannot reproduce the observed features, because it would provide different apparent source positions and different intensities and time profiles of the direct and reflected signals. Using numerical simulations, Kuznetsov et al. (2020) have recently demonstrated that the key factor in the formation of drift-pair bursts could be scattering of the emission on anisotropic plasma density fluctuations. The combination of reflection and anisotropic scattering (turbulent radio echo) has been shown to provide similar source sizes and locations and comparable intensities of the direct and reflected burst components, as well as to reproduce the source dynamics and the delays ($\sim 1-2$ s) between the components. This model also explains why drift-pair bursts are only observed below $\sim$ 100 MHz: at higher frequencies, the reflected component becomes damped due to collisional absorption. Thus anticipated high-quality observations of drift-pair bursts with SKA offer a fascinating opportunity to diagnose the plasma turbulence in the outer solar corona.

Besides, the origin of the emission itself remains unidentified yet. The emission is likely produced by non-thermal electrons as suggested by the high brightness temperatures; Interestingly, Kuznetsov and Kontar (2019) detected drift-pair bursts in absence of any flaring activity, while the emission source was located at a boundary of a coronal hole. Thus observations of drift-pair bursts can shed light on the magnetic reconnection and energy release processes in the otherwise quiet outer solar coronal regions, where solar wind acceleration begins. The frequency drift rates of drift-pair bursts are consistent with propagating MHD waves or whistler packets (see discussion Kuznetsov et al., 2020), and hence observations of the spatial, spectral, and temporal evolution of these bursts can be used to diagnose the magnetic field and plasma structures in their sources.

4 Type III striae

Type III bursts are a form of transient radio emission that quickly drifts from frequencies as high as hundreds of MHz or GHz down to as low as tens of kHz. The drift rate that scales approximately as

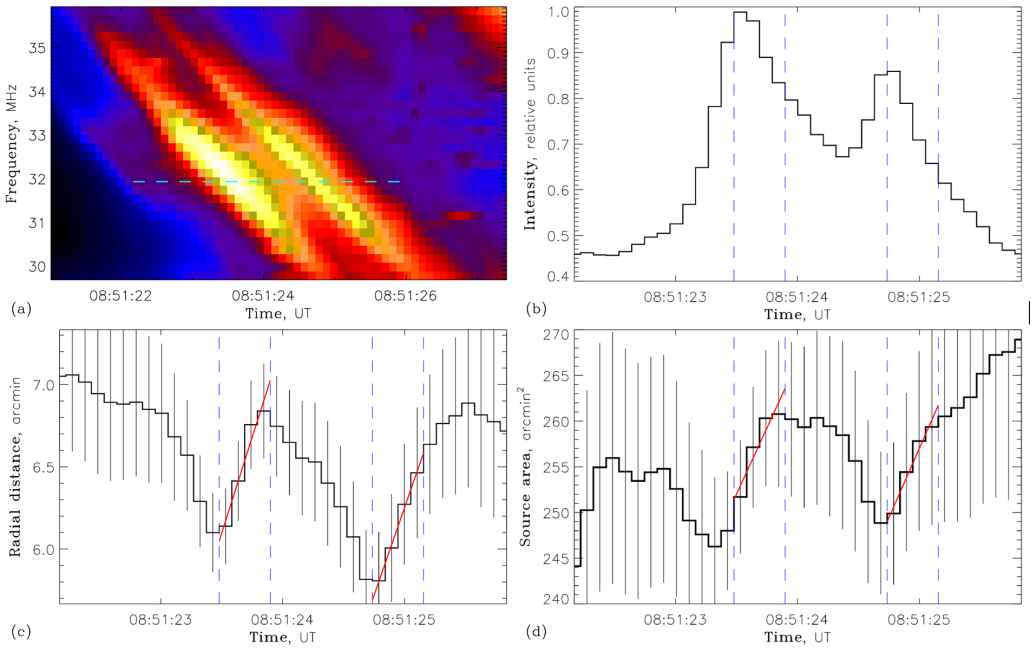

Figure 5: (a) Dynamic spectrum of solar radio emission with a drift-pair burst recorded with LOFAR on 2017 July 12 (Sun-integrated, in relative units). (b) Time profile of the radio flux at a single frequency (32 MHz). (c) Corresponding time profile of the visible radio source position (distance from the solar disk center). (d) Corresponding time profile of the visible radio source area (at half-maximum level). Red lines represent linear fits to the time profiles of the source parameters in the intervals shown. The error bars represent one standard deviation. Figure adapted from (Kuznetsov and Kontar, 2019).

$df/dt = 0.01 f^{1.84}$ (Alvarez and Haddock, 1973), is caused by energetic electrons propagating out from the Sun through plasma with the decreasing background plasma density of the solar corona and solar wind. Type III stria (Aubier et al., 1978; Abranin et al., 1979; Melnik et al., 2010), also known as type IIIb bursts (de La Noe and Boischot, 1972; Melnik et al., 2018; Kontar et al., 2017), are fine structures that are present within the bulk frequency drift of type III bursts. Stria are stripes in the dynamic spectra that drift slower than the type III burst ($df/dt \approx 0.1$ MHz s^{-1} at 30 MHz) with short durations (about 1 s at 30 MHz) and have a characteristic frequency bandwidth $\Delta f/f \approx 10^{-3}$, independent of frequency (Sharykin et al., 2018).

Stria are typically observed at frequencies above 10 MHz due to the higher resolution of ground-based telescopes, but have recently been observed below 1 MHz frequencies (Pulupa et al., 2020; Chen et al., 2021) and even below 100 kHz (Krupar et al., 2025). The source size of stria has been estimated to be 50-400 arcmin^2 around 25 and 40 MHz (Kontar et al., 2017; Chen et al., 2020; Zhang et al., 2020). The driver for type III stria is believed to be density turbulence in the background plasma (Takakura and Yousef, 1975). Enhanced resolutions obtained from LOFAR observations have found that the power spectral density of type III stria have a -5/3 spectral index for both fundamental and harmonic emission (Chen et al., 2018; Reid and Kontar, 2021), like the inertial range of density turbulence measured in the solar wind (Marsch, 1991; Bruno and Carbone, 2013). Power spectral densities detected in herringbone type II bursts have shown similar properties (Carley et al., 2021; Koval et al., 2023).

A theoretical framework for the generation of striae was provided by (Reid and Kontar, 2021), supported by numerical simulations. They demonstrated the fine structure could be caused by modulation in the growth rate of beam-driven Langmuir waves that in turn modulates the radio emission. The drift rate of stria is attributed to the motion of intense clumps of Langmuir waves in a turbulent medium, at the Langmuir wave group velocity $v_{gr} = 3v_{Te}/v_b$, where v_{Te} is the electron thermal velocity and v_b is the bulk speed of the electron beam. The intensity of radio emission can then be used to infer the level of density fluctuations parallel to the magnetic field via $\Delta I/I = (v_{Te}/v_b)^2 \Delta n/n$, where v_{Te} is the electron thermal speed and v_b is the electron beam speed. Values of $\Delta n/n = 3 \times 10^{-3}$ were found in the corona from stria, with similar (somewhat larger) values of $\Delta n/n = 8 \times 10^{-3}$ found from the fine structure in herringbones associated with a type II radio burst (Carley et al., 2021). Other studies have also approximated the level of density fluctuations $\delta n/n$ based upon the observed value of $\Delta f/f$ in stria, finding similar values from 10^{-2} to 10^{-3} (Mugundhan et al., 2017; Sharykin et al., 2018; Krupar et al., 2025). Anisotropic scattering of radio waves off density fluctuations has been shown to modify the properties of stria (Kontar et al., 2017, 2019; Chen et al., 2020). The scattering can cause a non-radial fixed-frequency source motion over time (Clarkson et al., 2023). Additionally, the apparent drift rate of stria can be reduced (Clarkson and Kontar, 2025), depending on the magnetic field direction and level of anisotropy of the density fluctuations.

5 Type II bursts fine structures

One of the most characteristic solar radio emissions are the so-called Type II radio bursts, displaying a much slower frequency-drift rate than other radio signatures ($\lesssim -1$ MHz s^{-1}; Wild, 1950). At decametric and metric wavelengths ($\gtrsim$10 MHz) they tend to have a life span of several minutes and relatively short instantaneous bandwidths. Type II bursts have been associated with shock waves traversing the heliosphere, normally driven by Coronal Mass Ejections (CMEs; e.g. Cliver et al., 1999). They also exhibit larger-scale structures, particularly band splitting—the separation of the Type II burst backbone into thinner, parallel lanes—and herringbones—Type-III-like bursts that appear to emanate from the backbone with opposing frequency-drift rates on each side (e.g. Roberts, 1959). However, fine structures within Type II bursts have also been identified since the very early observations, with Roberts (1959) noting that Type II bursts "are rarely smooth and continuous but fluctuate in intensity over periods of seconds", giving the appearance of a fragmented or patchy backbone (see Figure 6).

The mechanisms generating the larger-scale Type II structures (band splitting and herringbones) have been a source of long-standing debate (e.g. Smerd et al., 1974, 1975; Holman and Pesses, 1983; Mann and Klassen, 2005). There is no consensus on the mechanisms leading to the acceleration of energetic electrons and subsequent generation of radio emissions along shocks. Detailed studies of the finer and fainter structures observed within these Type II emissions could shed light onto the generation mechanisms responsible for the various morphologies. Thus, the ability to resolve and study these fine structures in detail (both spectroscopically and in images) is key to addressing these long-standing debates. The sensitivity of the SKA, along with the high temporal and spectral resolutions, and its ability to conduct imaging spectroscopy observations, will play an integral

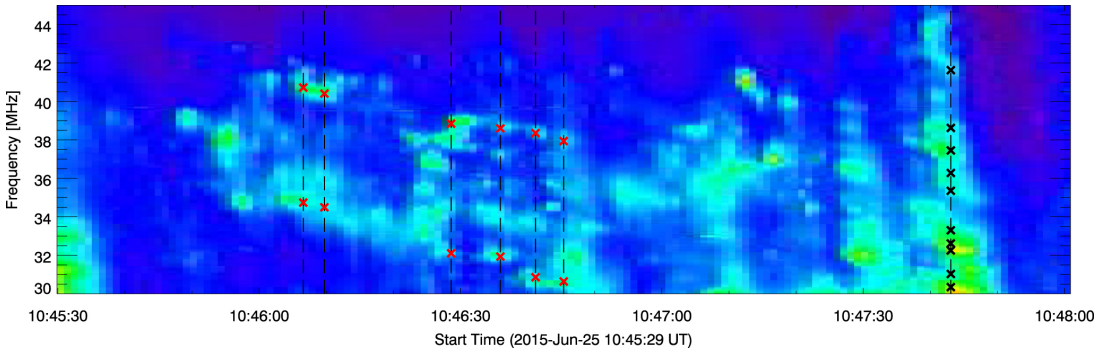

Figure 6: Type II solar radio burst exhibiting band splitting and highly-fragmented bands. LOFAR imaging spectroscopy observations allowed for the simultaneous imaging of both subbands at several moments in time, as shown by the red crosses. Figure taken from Chrysaphi et al. (2018) and reproduced by permission of the AAS.

role in such studies. Imaging spectroscopy is particularly beneficial as it allows us to identify the locations of the Type II radio emissions corresponding to each spectral measurement and explore the shock conditions and mechanisms that lead to the acceleration of electrons. For example, a major distinction in the two mainstream band-splitting models is whether the radio sources of the two subbands are co-spatial or physically separated along the shock (Smerd et al., 1974, 1975; Holman and Pesses, 1983). Due to instrumental limitations inducing time-delay ambiguities in the observations, it has been challenging to distinguish between the two scenarios. Chrysaphi et al. (2018) used LOFAR's imaging spectroscopy observations to conduct the first simultaneous imaging of both subbands of a split-band Type II burst (Figure 6), eliminating these ambiguities that prevented the simultaneous identification of the subband source locations.

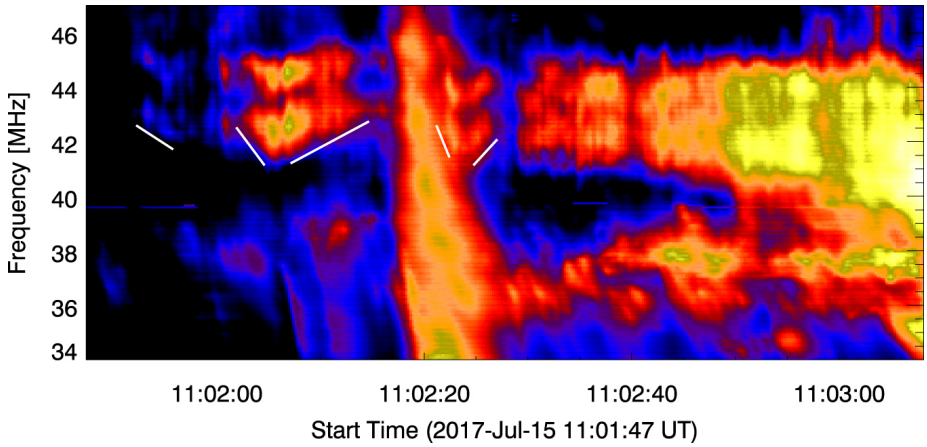

Figure 7: Intriguing fine structures observed within the stationary part of a Type II burst that transitions from a stationary to drifting state. The stationary parts of the Type II burst consist of two bands, both of which exhibit band splitting. The white-line annotations highlight fine structures that alternate between negative and positive frequency-drift rates. Figure taken from Chrysaphi et al. (2020) and reproduced under CC BY 4.0.

Observations and identifications of various fine structures embedded within Type II bursts have

increased with the commissioning of sensitive telescopes with very high temporal and spectral resolutions. Mann et al. (2018) used high-resolution observations by URAN-2 (Brazhenko et al., 2005) to examine the "head" and "tail" sub-structures of herringbones (Cairns and Robinson, 1987). Armatas et al. (2019) studied a large number of the spike-like fine structures observed within Type II bursts, recorded between 270–450 MHz by the ARTEMIS-IV (Kontogeorgos et al., 2006) spectrograph. They reported an average duration of 96 ms (with a standard deviation σ = 54 ms) and an average relative bandwidth of 1.7% (with σ = 0.5%). An intriguing behaviour of fine structures within the stationary part of a Type II burst that also exhibited band splitting was reported by Chrysaphi et al. (2020). This Type II burst—recorded with LOFAR and shown in Figure 7—transitioned from a stationary to drifting state, and displayed fine structures that alternate between positive and negative frequency-drift rates within the stationary part. Thanks to imaging spectroscopy observations, the Type II radio sources at various frequencies were imaged at sub-second intervals, revealing their spatial evolution, which aided in the identification of a generation mechanism. Overall, the SKA observations will facilitate the complete examination of Type II solar radio burst fine structures—which remain largely unexplored—advancing our ability to probe the shock-acceleration mechanisms and the impacts of propagation through the turbulent heliospheric medium.

Herringbone structures in type II solar radio bursts are often interpreted as direct signatures of electron acceleration at CME-driven shock fronts (Stewart, 1966; Cairns and Robinson, 1987; Mel'nik et al., 2004; Dorovskyy et al., 2015). In the dynamic spectrum (Figure 8), these structures appear as numerous short type III-like bursts that drift either to higher or lower frequencies, resembling fish bones branching off the main 'backbone'. The detailed properties of herringbones, such as their drift rates, durations, imaging locations, and polarization characteristics can provide insights into the underlying electron acceleration mechanisms.

6 Fine structures within flaring regions

The solar flare observations suggest a link between the X-ray emission and simultaneous radio emission. However, contrary to previous expectations decimetric spikes do not originate from coronal X-ray flare sources (Battaglia and Benz, 2009). This vision might be challenged by the future SKA-mid observations.

As the precursor to SKA-Mid, MeerKAT (Jonas and MeerKAT Team, 2016) has already conducted several successful solar flare observations, demonstrating its capability for stable calibration and high-fidelity spectroscopic imaging. The most recent imaging-spectroscopy study of a solar flare has shown that MeerKAT has already met, at least partially, several of the key solar flare requirements. Benefiting from its excellent *uv*-coverage and high sensitivity, the observations achieved high-fidelity imaging across the L band, revealing spatially distinct bright coherent sources (Figure 9), incoherent emission from hot coronal plasma, and even fainter diffuse components that remain invisible in AIA observations. The resulting images exhibit both high spatial resolution and good overall quality across the entire solar disk, demonstrating that MeerKAT can effectively image the full-Sun environment while resolving fine coronal structures. These results represent an advance compared with previous-generation radio arrays, establishing MeerKAT as a proof of concept for

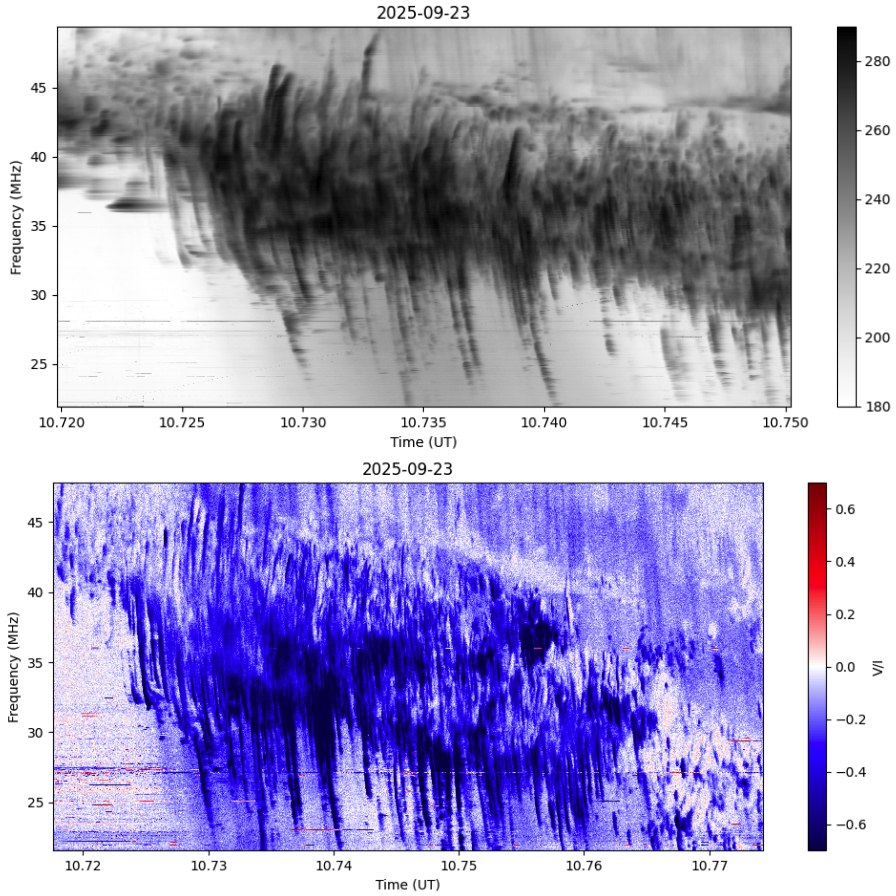

Figure 8: Type II solar radio burst exhibiting herringbone structures. *Top:* Stokes I dynamic spectrum *Top:* Polarization (Stokes V/I) dynamic spectrum. The spectra are from https://nenufar.obs-nancay.fr.

the next-generation SKA-Mid. Building on MeerKAT's demonstrated capabilities, SKA-Mid will take solar flare diagnostics with radio imaging spectroscopy to a fundamentally new level. With improved solutions for handling solar signal attenuation, SKA-Mid is expected to achieve imaging fidelity beyond that of the current generation of instruments. Crucially, this unprecedented image quality, combined with the potential for high temporal cadence, will enable flexible observing modes optimized for flare studies.

7 Solar observations and further progress

Radio observations provide powerful diagnostics of these processes through multiple emission mechanisms, each sensitive to flare-associated non-thermal electrons and their evolving coronal environments. Over the past decades, the development of imaging spectroscopy has led to revolutionary advances in flare studies (White et al., 2011). Current-generation interferometric arrays image each time-frequency pixel for both polarization products, allowing us to investigate spatially resolved sources and their temporal and spectral evolution in unprecedented detail, and to connect the observed emission structures with the underlying physical processes that govern energy release,

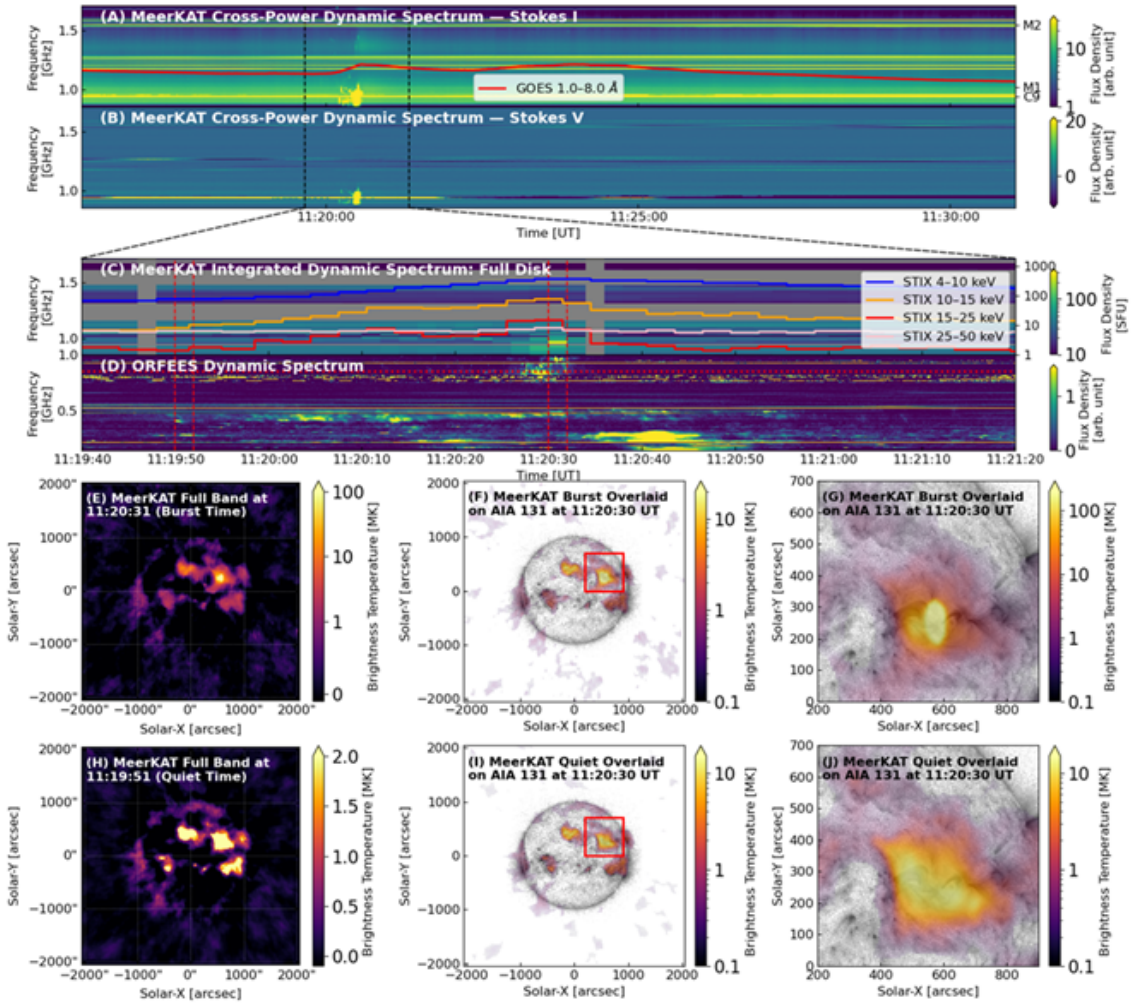

Figure 9: MeerKAT observations of fine structures in a solar flare by Luo et al. (2026). (A) MeerKAT Stokes I cross-power dynamic spectrum with GOES 1 – 8 Å soft X-ray flux (red) over-plotted. (B) MeerKAT Stokes V cross-power spectrum. (C) MeerKAT full-disk integrated dynamic spectrum during the burst with STIX light curves overlaid; bad channels and time intervals are flagged. (D) ORFEES (Hamini et al., 2021) dynamic spectrum. Vertical dashed black lines in (A) and (B) denote the interval shown in (C) and (D), while vertical dashed red lines in (C) and (D) mark the times used for imaging in (E)–(G) and (H)–(J). The red horizontal line in (D) indicates the low frequency limit of the MeerKAT band. (E) MeerKAT full-band radio image in brightness temperature (MK) at the burst peak, a linear colour scale for values below 1 MK and a logarithmic scale for values above 1 MK is used to enhance the visualization. (F) Alpha-blended overlay of MeerKAT emission (inferno colormap, transparency scaled by brightness) on an SDO/AIA (Lemen et al., 2012) 131 Å image (grayscale). Red boxes outline the regions shown in the zoomed-in view in (G). (H)–(J) Same as (E)–(G), but for the pre-burst quiet time.

particle acceleration, and transport in the corona.

However, to achieve further progress in flare diagnostics, several key limitations of current radio arrays must be addressed by future instruments. First, the available temporal resolution - even at the millisecond scale is often insufficient to resolve the shortest-lived coherent bursts (Luo et al.,

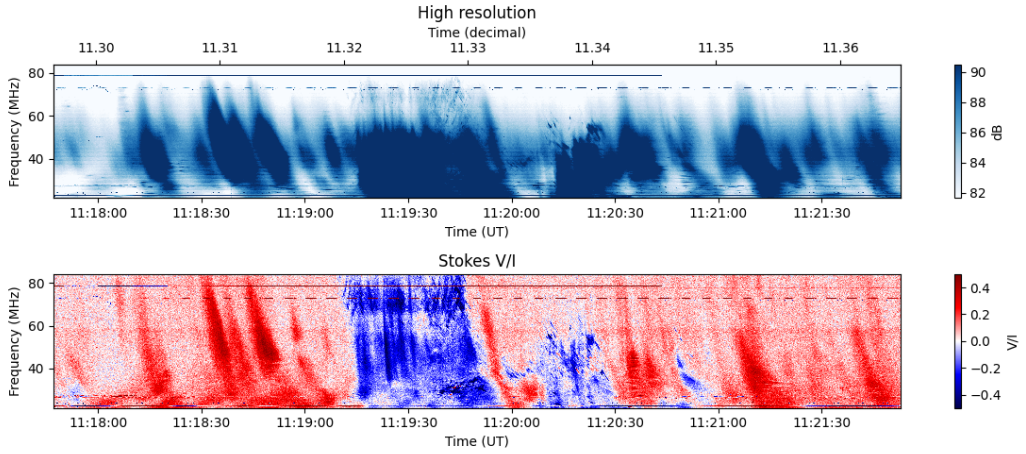

Figure 10: *Top:* Dynamic spectrum of solar radio emission observed by NenuFAR on 2024 July 11 (Sun-integrated, in relative units). *Bottom:* Polarization of the same time interval showing reverse of polarization around 11:19:30 UT. The spectra are from https://nenufar.obs-nancay.fr.

2026), whose rapid evolution contains critical information about the transport of energetic electrons and their interaction with the surrounding plasma. Second, high spatial resolution combined with a sufficiently wide field of view is required, so that fine coronal structures can be resolved while simultaneously covering the entire solar disk and the overlying corona extending to at least several solar radii. Third, improved *uv*-coverage is essential for producing high-fidelity synthesis images that enable the investigation of multiple spatially distinct and spectrally different sources evolving simultaneously during flares. In addition, broad and continuous frequency coverage, together with accurate full-polarization calibration, is crucial for distinguishing between different emission mechanisms and for deriving quantitative diagnostics of the energetic electron population and the coronal magnetic environment. Figure 10 shows that while Stokes I do not display much difference, the polarization signal indicates that the conditions of emission completely changed. Finally, solar-dedicated calibration schemes and observing operations are also essential to ensure stable performance during high-intensity solar observations.

For example, beam-formed modes may deliberately trade a modest amount of image fidelity for substantially improved temporal and frequency resolutions. Given SKA intrinsically high imaging performance (Figure 9), such a trade-off is expected to be highly advantageous for flare diagnostics (Luo et al., 2026). The inclusion of the outer antennas will further enhance the *uv*-coverage, providing much better spatial resolution for resolving fine coronal structures and improved sensitivity to faint, extended features. Together, these advances will enable investigations of radio sources at previously unattainable temporal and spatial resolution. The SKA will open new opportunities for advances in key science areas-particularly particle acceleration and transport, the associated magnetic reconnection and energy release processes at the shorter scales than available before, and the subsequent energy transformation and coupling between non-thermal electrons and the heated plasma.

Another tantalizing opportunity stems from the interplanetary bursts, where variations in type

III radio burst drift rates could be caused by magnetic-field direction changes, not just density inhomogeneities (Clarkson and Kontar, 2026). Many observables like drift-rate reductions, delays, and fine structure to be observed with the SKA could be natural consequences of beam propagation along disturbed magnetic fields, especially magnetic switchback-like structures, the topic poorly understood in solar physics.

8 Summary

Frequency-time-resolved imaging observations of solar radio bursts has brought a qualitatively new look at solar phenomena. The solar radio burst images are found to change at sub-second scales: the centroid locations at a given frequency are moving often with superluminal speeds, and the angular extent of the radio sources at a given frequency is also evolving with time. Often, the images are likely to be due to scattering, but the variation of image size from one burst type to another suggests that we do not fully understand all processes responsible for the source size variations.

Evidently the observations at selected frequencies are unable to shed light on the origin of the fine time-frequency structure of solar radio emission. The lack or absence of imaging information often makes it impossible to understand the origin of the fine structures.

A handful of observations able to resolve time-frequency structures strongly suggests the diagnostic potential of radio emission from 50 MHz to 10 GHz range is not fully explored. The SKA will improve our understanding of the fine structure of solar radio bursts, by providing much needed imaging information on the locations and sizes of the sources over a broad range of frequencies. As all solar corona sources are embedded into magnetized turbulent plasma, the escape of radio emission is an important consideration to make.

9 Acknowledgements

This work is partially supported by the Leverhulme Trust (Research Fellowship RF-2025-357) and STFC/UKRI grant ST/Y001834/1. We acknowledge support from the International Space Science Institute for the LOFAR team http://www.issibern.ch/teams/lofar/. This work has made use of NASA's Astrophysics Data System Bibliographic Services. N. Chrysaphi was supported by the Space It Up! project, funded by the Italian Space Agency (ASI) and the Ministry of University and Research (MUR), under contract No. 2024-5-E.0–CUP I53D24000060005.

References

E. P. Abranin et al. Sol. Phys., 62(1):145–151, May 1979. doi: 10.1007/BF00150141.

H. Alvarez and F. T. Haddock. Sol. Phys., 29(1):197–209, Mar. 1973. doi: 10.1007/BF00153449.

S. Armatas et al. A&A, 624:A76, Apr. 2019. doi: 10.1051/0004-6361/201834982.

M. G. Aubier, Y. Leblanc, and B. Moller-Pedersen. A&A, 70:685, Nov. 1978.

C. H. Barrow, P. Zarka, and M. G. Aubier. A&A, 286:597–606, June 1994.

M. Battaglia and A. O. Benz. A&A, 499(3):L33–L36, June 2009. doi: 10.1051/0004-6361/200912143.

A. O. Benz. Sol. Phys., 96(2):357–370, Apr. 1985. doi: 10.1007/BF00149690.
A. O. Benz. *Living Reviews in Solar Physics*, 14(1):2, Dec. 2017. doi: 10.1007/s41116-016-0004-3.
A. O. Benz, M. Jaeggi, and P. Zlobec. A&A, 109(2):305–313, May 1982.
A. O. Benz, H. Su, A. Magun, and W. Stehling. A&AS, 93(3):539–544, June 1992.
C. Bouratzis et al. A&A, 586:A29, Feb. 2016. doi: 10.1051/0004-6361/201527229.
R. Braun et al. Anticipated performance of the square kilometre array – phase 1 (ska1), 2019. URL https://arxiv.org/abs/1912.12699.
A. I. Brazhenko et al. *Kinematika i Fizika Nebesnykh Tel Supplement*, 5:43–46, June 2005.
R. Bruno and V. Carbone. *Living Reviews in Solar Physics*, 10(1):2, Dec. 2013. doi: 10.12942/lrsp-2013-2.
I. H. Cairns and R. D. Robinson. Sol. Phys., 111(2):365–383, Sept. 1987. doi: 10.1007/BF00148526.
E. P. Carley et al. ApJ, 921(1):3, Nov. 2021. doi: 10.3847/1538-4357/ac1acd.
A. P. Cerruti et al. *Space Weather*, 6(10):S10D07, Oct. 2008. doi: 10.1029/2007SW000375.
B. Chen et al. *Science*, 350(6265):1238–1242, Dec. 2015. doi: 10.1126/science.aac8467.
L. Chen et al. ApJ, 915(1):L22, July 2021. doi: 10.3847/2041-8213/ac0b43.
X. Chen et al. ApJ, 856(1):73, Mar. 2018. doi: 10.3847/1538-4357/aaa9bf.
X. Chen et al. ApJ, 905(1):43, Dec. 2020. doi: 10.3847/1538-4357/abc24e.
G. P. Chernov. *Fine Structure of Solar Radio Bursts*, volume 375. Springer-Verlag Berlin Heidelberg, 2011. doi: 10.1007/978-3-642-20015-1.
N. Chrysaphi, E. P. Kontar, G. D. Holman, and M. Temmer. ApJ, 868(2):79, Dec 2018. doi: 10.3847/1538-4357/aae9e5.
N. Chrysaphi, H. A. S. Reid, and E. P. Kontar. ApJ, 893(2):115, Apr. 2020. doi: 10.3847/1538-4357/ab80c1.
D. L. Clarkson and E. P. Kontar. ApJ, 978(1):73, Jan. 2025. doi: 10.3847/1538-4357/ad969c.
D. L. Clarkson and E. P. Kontar. ApJ, 999(1):134, Mar. 2026. doi: 10.3847/1538-4357/ae3dae.
D. L. Clarkson et al. ApJ, 917(2):L32, Aug. 2021. doi: 10.3847/2041-8213/ac1a7d.
D. L. Clarkson et al. ApJ, 946(1):33, Mar. 2023. doi: 10.3847/1538-4357/acbd3f.
E. W. Cliver, D. F. Webb, and R. A. Howard. Sol. Phys., 187(1):89–114, June 1999. doi: 10.1023/A:1005115119661.
E. W. Cliver, S. M. White, and K. S. Balasubramaniam. ApJ, 743(2):145, Dec. 2011. doi: 10.1088/0004-637X/743/2/145.
J. de La Noe and A. Boischot. A&A, 20:55, Aug. 1972.
B. R. Dennis, A. G. Emslie, and H. S. Hudson. Space Sci. Rev., 159(1-4):3–17, Sept. 2011. doi: 10.1007/s11214-011-9802-z.
B. P. Dąbrowski, P. Rudawy, and M. Karlický. Sol. Phys., 273(2):377–392, Nov. 2011. doi: 10.1007/s11207-011-9756-z.
V. V. Dorovskyy et al. Sol. Phys., 290(7):2031–2042, July 2015. doi: 10.1007/s11207-015-0725-9.
M. Gordovskyy et al. ApJ, 925(2):140, Feb. 2022. doi: 10.3847/1538-4357/ac3bb7.
M. Guedel and A. O. Benz. A&A, 231(1):202–212, May 1990.
M. Guedel, A. O. Benz, and M. J. Aschwanden. A&A, 251(1):285–297, Nov. 1991.
A. Hamini et al. *Journal of Space Weather and Space Climate*, 11:57, Oct. 2021. doi: 10.1051/swsc/2021039.

G. A. Hampson et al. *Journal of Astronomical Telescopes, Instruments, and Systems*, 8:011018, Jan. 2022. doi: 10.1117/1.JATIS.8.1.011018.

G. D. Holman and M. E. Pesses. ApJ, 267:837–843, Apr. 1983. doi: 10.1086/160918.

G. D. Holman et al. Space Sci. Rev., 159(1-4):107–166, Sept. 2011. doi: 10.1007/s11214-010-9680-9.

J. Jonas and MeerKAT Team. In *MeerKAT Science: On the Pathway to the SKA*, page 1, Jan. 2016. doi: 10.22323/1.277.0001.

P. M. Kintner, B. O'Hanlon, D. E. Gary, and P. M. S. Kintner. *Radio Science*, 44(2):RS0A08, June 2009. doi: 10.1029/2008RS004039.

E. P. Kontar et al. Space Sci. Rev., 159(1-4):301–355, Sept. 2011. doi: 10.1007/s11214-011-9804-x.

E. P. Kontar et al. *Nature Communications*, 8:1515, Nov. 2017. doi: 10.1038/s41467-017-01307-8.

E. P. Kontar et al. ApJ, 884(2):122, Oct. 2019. doi: 10.3847/1538-4357/ab40bb.

E. P. Kontar et al. ApJ, 956(2):112, Oct. 2023. doi: 10.3847/1538-4357/acf6c1.

E. P. Kontar, A. G. Emslie, D. L. Clarkson, and A. Pitňa. ApJ, 991(2):L57, Oct. 2025. doi: 10.3847/2041-8213/ae09b0.

A. Kontogeorgos et al. *Experimental Astronomy*, 21(1):41–55, Feb. 2006. doi: 10.1007/s10686-006-9066-x.

A. Koval et al. ApJ, 952(1):51, July 2023. doi: 10.3847/1538-4357/acdbcc.

S. Krucker and A. O. Benz. A&A, 285:1038–1046, May 1994.

S. Krucker, M. J. Aschwanden, T. S. Bastian, and A. O. Benz. A&A, 302:551, Oct. 1995.

V. Krupar et al. ApJ, 985(2):L27, June 2025. doi: 10.3847/2041-8213/add688.

A. A. Kuznetsov and E. P. Kontar. A&A, 631:L7, Nov. 2019. doi: 10.1051/0004-6361/201936447.

A. A. Kuznetsov, N. Chrysaphi, E. P. Kontar, and G. Motorina. ApJ, 898(2):94, Aug. 2020. doi: 10.3847/1538-4357/aba04a.

J. R. Lemen et al. Sol. Phys., 275(1-2):17–40, Jan. 2012. doi: 10.1007/s11207-011-9776-8.

Y. Luo et al. ApJ, 911(1):4, Apr. 2021. doi: 10.3847/1538-4357/abe5a4.

Y. Luo et al. ApJ, 998(2):L46, Feb. 2026. doi: 10.3847/2041-8213/ae42c1.

S. Ma et al. *arXiv e-prints*, art. arXiv:2605.23484, May 2026. doi: 10.48550/arXiv.2605.23484.

G. Mann and A. Klassen. A&A, 441(1):319–326, Oct. 2005. doi: 10.1051/0004-6361:20034396.

G. Mann et al. A&A, 609:A41, Jan 2018. doi: 10.1051/0004-6361/201730546.

E. Marsch. *Reviews in Modern Astronomy*, 4:145–156, Jan. 1991. doi: 10.1007/978-3-642-76750-0_10.

V. N. Mel'nik et al. Sol. Phys., 222(1):151–166, July 2004. doi: 10.1023/B:SOLA.0000036854.66380.a4.

V. N. Melnik et al. In S. K. Chakrabarti, A. I. Zhuk, and G. S. Bisnovatyi-Kogan, editors, *American Institute of Physics Conference Series*, volume 1206 of *American Institute of Physics Conference Series*, pages 445–449. AIP, Jan. 2010. doi: 10.1063/1.3292552.

V. N. Melnik et al. Sol. Phys., 289(5):1701–1714, May 2014. doi: 10.1007/s11207-013-0434-1.

V. N. Melnik et al. Sol. Phys., 293(2):26, Feb. 2018. doi: 10.1007/s11207-017-1234-9.

D. B. Melrose and G. A. Dulk. ApJ, 259:844–858, Aug. 1982. doi: 10.1086/160219.

V. Mugundhan, K. Hariharan, and R. Ramesh. Sol. Phys., 292(11):155, Nov. 2017. doi: 10.1007/s11207-017-1181-5.

P. C. Murphy et al. *The Open Journal of Astrophysics*, 7:51, June 2024. doi: 10.33232/001c.120317.

V. Nakariakov et al. In *Advancing Astrophysics with the Square Kilometre Array (AASKA14)*, page 169, Apr. 2015. doi: 10.22323/1.215.0169.

A. Nindos, E. P. Kontar, and D. Oberoi. *Advances in Space Research*, 63(4):1404–1424, Feb. 2019. doi: 10.1016/j.asr.2018.10.023.

M. Pulupa et al. ApJS, 246(2):49, Feb. 2020. doi: 10.3847/1538-4365/ab5dc0.

H. A. S. Reid and E. P. Kontar. *Nature Astronomy*, 5:796–804, May 2021. doi: 10.1038/s41550-021-01370-8.

J. A. Roberts. *Australian Journal of Physics*, 11:215, June 1958. doi: 10.1071/PH580215.

J. A. Roberts. *Australian Journal of Physics*, 12:327, Dec 1959. doi: 10.1071/PH590327.

I. N. Sharykin, E. P. Kontar, and A. A. Kuznetsov. Sol. Phys., 293(8):115, Aug. 2018. doi: 10.1007/s11207-018-1333-2.

N. V. Shevchuk et al. Sol. Phys., 291(1):211–228, Jan. 2016. doi: 10.1007/s11207-015-0799-4.

S. F. Smerd, K. V. Sheridan, and R. T. Stewart. In G. A. Newkirk, editor, *Coronal Disturbances*, volume 57 of *IAU Symposium*, page 389, 1974.

S. F. Smerd, K. V. Sheridan, and R. T. Stewart. Astrophys. Lett., 16:23–28, 1975.

M. Staehli and A. Magun. Sol. Phys., 104(1):117–123, Mar. 1986. doi: 10.1007/BF00159952.

R. T. Stewart. *Australian Journal of Physics*, 19:209, Apr. 1966. doi: 10.1071/PH660209.

S. Suzuki and D. E. Gary. PASA, 3(5-6):379–383, Jan. 1979. doi: 10.1017/S1323358000026151.

T. Takakura and S. Yousef. Sol. Phys., 40(2):421–438, Feb. 1975. doi: 10.1007/BF00162389.

G. L. Tarnstrom and K. W. Philip. A&A, 16:21, Jan. 1972a.

G. L. Tarnstrom and K. W. Philip. A&A, 17:267, Mar. 1972b.

M. P. van Haarlem et al. A&A, 556:A2, Aug. 2013. doi: 10.1051/0004-6361/201220873.

S. M. White et al. Space Sci. Rev., 159(1-4):225–261, Sept. 2011. doi: 10.1007/s11214-010-9708-1.

J. P. Wild. *Australian Journal of Scientific Research A Physical Sciences*, 3:399, Sept. 1950. doi: 10.1071/PH500399.

P. Zhang et al. A&A, 639:A115, July 2020. doi: 10.1051/0004-6361/202037733.